AGU PUBLICATIONS

Tectonics

RESEARCH ARTICLE
10.1002/2017TC004673

Special Section:
The 2016 Central Italy Seismic Sequence: Insights, Implications and Lessons Learned

Imprint of Rupture Directivity From Ground Motions of the 24 August 2016 M_w6.2 Central Italy Earthquake

Yefei Ren[1], **Hongwei Wang**[1], **and Ruizhi Wen**[1]

[1]Key Laboratory of Earthquake Engineering and Engineering Vibration of China Earthquake Administration, Institute of Engineering Mechanics, China Earthquake Administration, Harbin, China

Key Points:

- Imprint of rupture directivity in the 24 August 2016 Central Italy earthquake has been revealed using the strong motion recordings
- Rupture directivity had considerable effects on azimuthal variations of observed PGAs, PGVs, and short-period PSAs
- Inverted source parameters confirmed that the rupture propagated predominantly unilaterally in the NNW direction

Abstract An M_w6.2 earthquake occurred in Central Italy on 24 August 2016. The objective of this study was to reveal the imprint of rupture directivity using the strong motion recordings. The strong motion stations were separated into two groups: southeast (SE) and northwest (NW). The effects of rupture directivity on the peak ground acceleration (PGA), peak ground velocity (PGV), and pseudo spectral acceleration (PSA) were investigated. The observed values of these parameters were compared with predicted values derived from ground motion prediction equations. The results showed that the residuals between the observed and predicted PGAs, PGVs, and PSAs at periods of $T < 1$ s were correlated significantly with azimuth angle and generally larger in the NW sector, reflecting that the observed PGAs, PGVs, and short-period PSAs in the NW sector were generally larger than observed in the SE sector. These phenomena are accordant with the theoretical law that the rupture directivity causes higher amplitudes in the forward direction compared with the backward direction. Finally, selected source rupture parameters were inverted using PGAs and PGVs. This revealed that the rupture was predominantly unilateral rupture, the major rupture was likely at an azimuth of ~360°, and the length of the major rupture was proportional to 70%–100% of the total ruptured fault, confirming that rupture directivity caused the differences in the ground motions observed in the SE and NW sectors.

1. Introduction

It is well known that the spatial distribution of ground motions is influenced by the source radiation pattern, source-to-site propagation path, and local site effects. In an M_w7.5 earthquake that occurred in 1952 in Kern County, California (USA), the long-period ground motions reflected the strong dependence of the radiation energy on azimuth, which might have been attributable to the asymmetry of rupture propagation between the forward and backward directions (Benioff, 1955). When a rupture propagates predominantly in a single direction from nucleation, the resulting ground motion can be subjected to a dramatic azimuthal effect, commonly referred to as the directivity effect. It induces the most severe ground motion in the direction of the predominant rupture, which is characterized by higher amplitudes and shorter durations (Somerville et al., 1997).

Significant directivity effects have been recognized in large numbers of destructive earthquakes, e.g., the 28 June 1992 M_w7.3 Landers earthquake in California (USA) (Velasco, Ammon, & Lay, 1994), 17 January 1994 M_w6.7 Northridge earthquake in California (USA) (Somerville, Graves, & Smith, 1996), 17 January 1995 M_w6.9 Kobe earthquake in Japan (Somerville et al., 1996), 21 September 1999 M_w7.7 Chi-Chi earthquake in Taiwan (Phung, Atkinson, & Lau, 2004), and 12 May 2008 M_w7.8 Wenchuan earthquake in Sichuan (China) (Hu & Xie, 2011). The directivity effect on ground motions has also been observed in some small-to-moderate earthquakes in recent years, e.g., the 2011 M_w5.2 Lorca earthquake in Spain (López-Comino et al., 2012), 2003 Big Bear sequence in Southern California (USA) (Tan & Helmberger, 2010), and 2013 Lushan aftershocks in China (Wen, Wang, & Ren, 2015). Analysis of such evidence could improve the understanding of rupture directivity within the earthquake engineering community, which could lead to the development of directivity predictions for ground motion prediction equations (GMPEs) (Spudich et al., 2014).

On 24 August 2016 at 01:36:32 UT, an M_w6.2 (provided by U.S. Geological Survey) earthquake occurred in the Central Apennines (Italy) between the towns of Norcia and Amatrice, causing nearly 300 fatalities and considerable economic loss. This followed the 2009 M_w6.3 L'Aquila earthquake, which was another devastating

Correspondence to:
R. Wen,
ruizhi@iem.ac.cn

Citation:
Ren, Y., Wang, H., & Wen, R. (2017). Imprint of rupture directivity from ground motions of the 24 August 2016 M_w6.2 Central Italy earthquake. *Tectonics*, *36*, 3178–3191. https://doi.org/10.1002/2017TC004673

Received 24 MAY 2017
Accepted 14 NOV 2017
Accepted article online 27 NOV 2017
Published online 20 DEC 2017

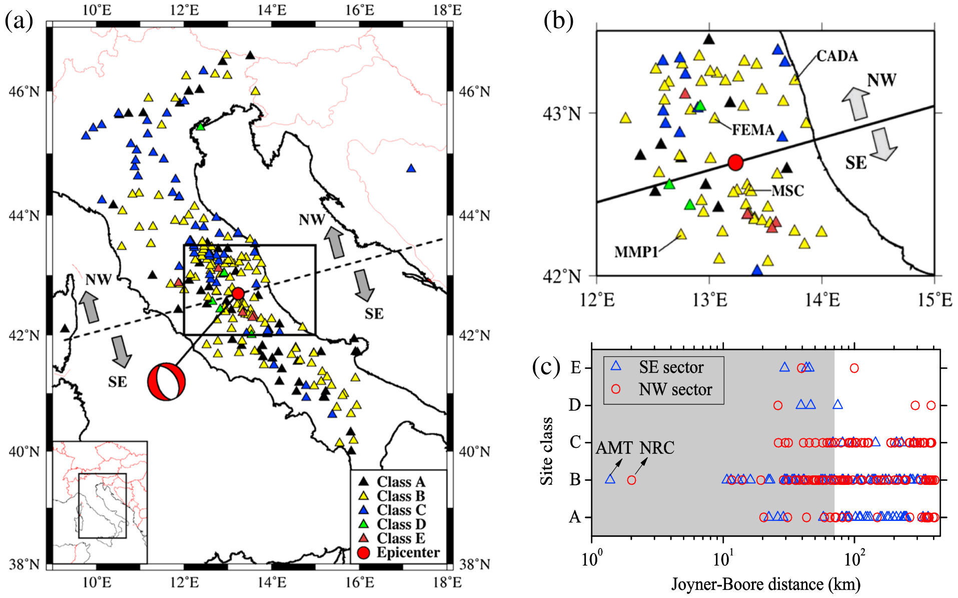

Figure 1. (a) The triggered stations in the M_w6.2 earthquake that occurred in Central Italy on 24 August 2016. The dashed line passing through the epicenter (red circle), perpendicular to the NNW-SSE trending seismogenic fault (165°), was used to separate the stations into the NW and SE groups. The focal mechanism plotted was provided by the U.S. Geological Survey. The triangles of different colors represent the different site classes as defined in Eurocode 8. (b) Stations with $R_{JB} < 70$ km. Two pairs of stations are highlighted: FEMA and MSC, and CADA and MMP1. The locations of both stations in each pair are symmetrical with respect to the boundary line between the NW and SE sectors. (c) Distribution of Joyner-Boore distances for stations with respect to each site class, i.e., Classes A–E. Note that the numbers of stations with $R_{JB} < 70$ km (shaded area) in the NW and SE sectors are almost the same for Classes A and B.

event in Italy. Both earthquakes occurred on the same seismic fault belt. The epicenter of the 2016 event was located 45 km northwest of the L'Aquila event. Rupture directivity in the L'Aquila event was confirmed by the systematic decrease of peak ground accelerations (PGAs) and peak ground velocities (PGVs) at sites located in the backward direction of rupture propagation (Akinci, Malagnini, & Sabetta, 2010). The predominantly unilateral rupture directivity of the L'Aquila earthquake was also confirmed by slip inversions (Cirella et al., 2012; Gallovič, Imperatori, & Martin Mai, 2015). For the 2016 event, based on kinematic slip inversions, studies by Tinti et al. (2016), Chiaraluce et al. (2017), and Pizzi et al. (2017) suggested bilateral rupture propagation, with perhaps more distinct propagation toward the northwest. Within this context, the objective of this study was to investigate the imprint of rupture directivity based on the ground motion intensity measures (IMs) of the 2016 event. It should be noted that this study was concerned only with the first main shock (24 August 2016), even though two subsequent large events occurred as part of this earthquake sequence, i.e., M_w5.9 on 26 October and M_w6.5 on 30 October (Chiaraluce et al., 2017; Pizzi et al., 2017).

Many strong motion recordings were collected during this event by the Italian Accelerometric Network (RAN) and the Italian Seismic Network (RSN). In particular, the data observed at many sites located in the near field of the ruptured fault allowed us to investigate the effects of rupture directivity on IMs such as PGA, PGV, and 5% damped pseudo spectral accelerations (PSAs) at different spectral periods. Finally, selected rupture parameters, e.g., rupture velocity, dominant horizontal rupture direction, and percent of unilateral rupture, were estimated using an inversion technique based on the observed PGA and PGV fields.

2. Data

More than 260 strong motion recordings collected during the 2016 event are available from the Engineering Strong-Motion database (ESM, esm.mi.ingv.it). Most were recorded at stations belonging to RAN and RSN. The locations of the stations are shown in Figure 1a, where the site classes, as defined in Eurocode 8, are distinguished by the different colored triangles. All the data provided by ESM are preelaborations, including processed acceleration, velocity, displacement time histories, and response spectra.

To investigate the differences in ground motions in the forward and backward directions of rupture propagation, the stations were separated into two groups (NW and SE) according to a line perpendicular to the NNW-SSE trending seismogenic fault (165°) across the epicenter. A fault plane striking 165° and dipping 45° toward the WSW was released by the U.S. Geological Survey. The Istituto Nazionale di Geofisica e Vulcanologia (INGV) provided another fault geometry distribution with strike angle of 155° and dip angle of 49°. However, irrespective of which was used in this study, the effect on the results concerning rupture directivity would be small. This is because the boundary (dashed line in Figure 1a) would be changed by a rotation of only 10°, which would not cause significant variation of the station distribution with respect to the NW and SE groups.

To investigate rupture directivity, 76 sites located at the Joyner–Boore distance (R_{JB}) lower than 70 km (Figure 1b) were specifically selected: 35 located in the SE sector and 41 in the NW sector. The R_{JB} values of all sites, derived directly from ESM, were calculated based on the geometry data of the fault plane inverted by Tinti et al. (2016). In the previous L'Aquila event, the ground motions from sites located at epicentral distances smaller than 70 km reflected a prominent directivity effect (Akinci et al., 2010). It should be noted that two stations, AMT in the SE sector and NRC in the NW sector with R_{JB} = 1–2 km were excluded in this study, because their waveforms could be unwantedly affected by the details of the rupture process, such as the locations of asperities and updip directivity. The availability of almost the same number of sites in both sectors makes this investigation possible. The R_{JB} distribution for stations with respect to their site classes is shown in Figure 1c. It shows that most stations are Class A and B sites, and the number of stations is almost the same in both sectors. This could reduce the potential impact of local site effects on the investigation of the influence of rupture directivity on ground motions.

3. Characteristics of Observed Ground Motions

To investigate the potential effects of rupture directivity on ground motions, we compared the ground motion IMs observed in the NW and SE sectors, including PGA, PGV, and 5% damped PSA. The geometric mean of two orthogonal horizontal components was taken as representative for one site. We compared the observed values of these IMs with values predicted by GMPEs.

3.1. Peak Ground Motion Parameters

The observed PGAs and PGVs were compared with the predicted values estimated by three GMPEs developed by Bindi et al. (2011) (called Bin11), Akkar and Bommer (2007a) (called AB07a), and Akkar and Bommer (2007b) (called AB07b). Bin11 was derived from the Italian strong motion database, and it could be used for predicting PGA, PGV, and 5% damped spectral accelerations at periods between 0.04 and 2.00 s. AB07a could be used for predicting PGA and displacement response ordinates for different damping ratios at periods up to 4.00 s. AB07b could be used for predicting only PGV. Both AB07a and AB07b were derived from the strong motion database for the seismically active areas of Europe and the Middle East. In this study, PGAs were estimated using Bin11 and AB07a, and PGVs were estimated using Bin11 and AB07b.

Figures 2 and 3 show comparisons of the PGAs and PGVs, respectively, between the observed and predicted values and their residuals. The total residual (Res) is given by

$$\mathrm{Res} = \log 10\left(\mathrm{IM}_{\mathrm{obs}}/\mathrm{IM}_{\mathrm{pred}}\right), \tag{1}$$

where $\mathrm{IM}_{\mathrm{obs}}$ and $\mathrm{IM}_{\mathrm{pred}}$ represent the observed and predicted ground motion IMs, respectively. The positive (or negative) residual represents an underprediction (or overprediction) of the IMs. The total residual could be decomposed into between-event and within-event residuals, as proposed by Al Atik et al. (2010). The between-event residual represents the earthquake-to-earthquake variability. For an individual earthquake, all recordings include the same event term. The within-event residual represents the record-to-record variability, i.e., azimuthal variations in source, path, and site effects. To investigate the only azimuthal variations in the source (i.e., rupture directivity), the path-corrected residual was used in this study, which was calculated as the total residual minus its distance-binned mean, as shown in Figures 2 and 3 (bottom row). Binned means of the total residuals were calculated for R_{JB} ranges of 0–50, 50–100, 100–200, and 200–400 km, as shown in Figures 2 and 3 (middle row). We note that several values of moment magnitude for this Central Italy earthquake have been released, e.g., M_w6.2 by the U.S. Geological Survey and Pizzi et al. (2017), M_w6.1

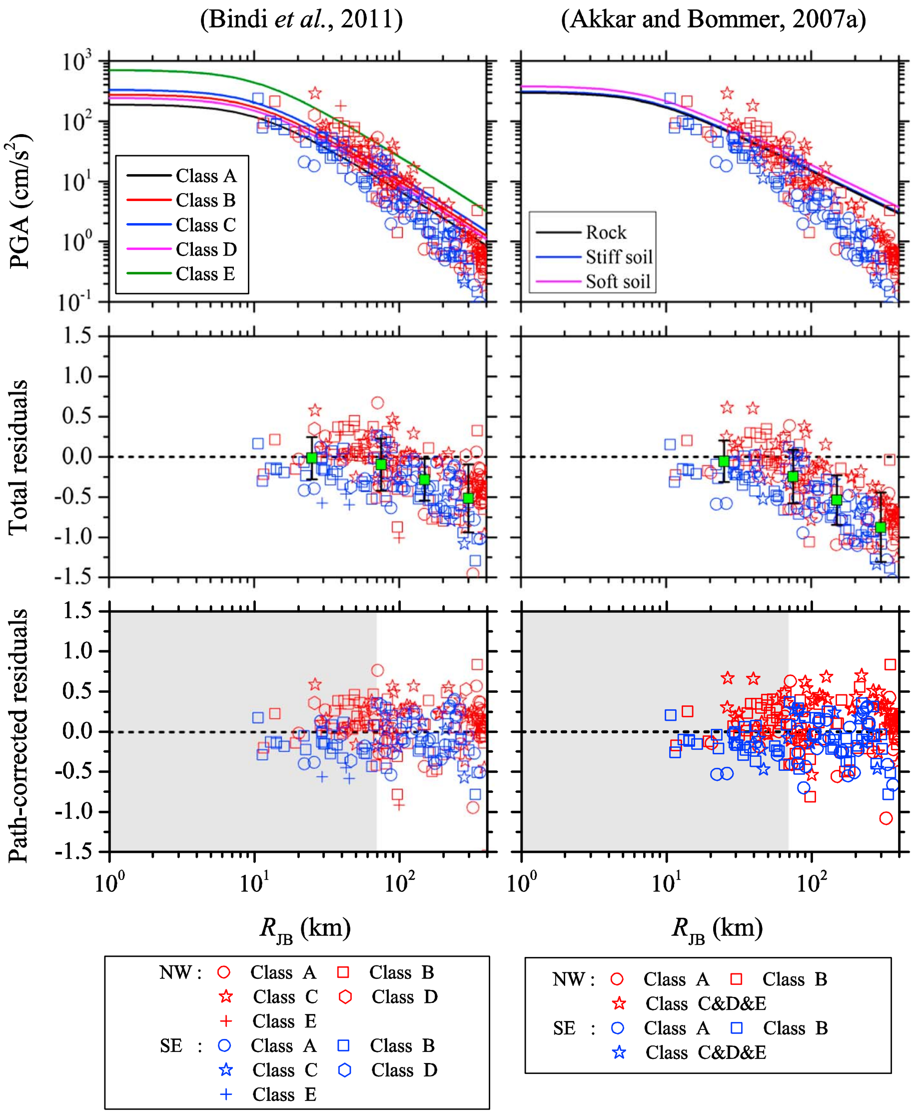

Figure 2. Comparisons of the observed and predicted PGAs and of their residuals. The predicted values were calculated using the GMPEs developed by Bindi et al. (2011) and Akkar and Bommer (2007a). (middle row) The green filled squares with bars, indicating standard errors, are binned means of the total residuals for R_{JB} ranges of 0–50, 50–100, 100–200, and 200–400 km. (bottom row) The path-corrected residuals are plotted, which were calculated as the total residuals minus their distance-binned means. The shaded areas show the R_{JB} range (i.e., <70 km) within which the sites were used specifically to investigate the directivity effects.

by Tinti et al. (2016), and M_w6.0 by INGV; the value of $M_w = 6.2$ was considered in this study. Obviously, uncertainty regarding the magnitude could affect the IM predictions and their total residuals. However, the path-corrected residual implicitly removes the impact of magnitude uncertainty. Therefore, irrespective of the value of M_w used, the identification of rupture directivity based on the analyses of ground motion IMs would be unchanged.

To characterize the site effect term in both AB07a and AB07b, the sites were classified as rock, stiff soil, and soft soil, according to the average shear-wave velocity over the uppermost 30 m at the site (V_{S30}). A V_{S30} value above 750 m/s corresponds to rock, below 360 m/s corresponds to soft soil, and an intermediate value corresponds to stiff soil. According to the defined range of V_{S30} for each site class in Eurocode 8, Class A ($V_{S30} > 800$ m/s) is approximately equivalent to rock, Class B ($V_{S30} = 360$–800 m/s) is equivalent to stiff soil, and Classes C–E ($V_{S30} < 360$ m/s) are together equivalent to soft soil. For Bin11, the five types of site class defined in Eurocode 8 (Classes A–E) were used for characterizing different site amplifications.

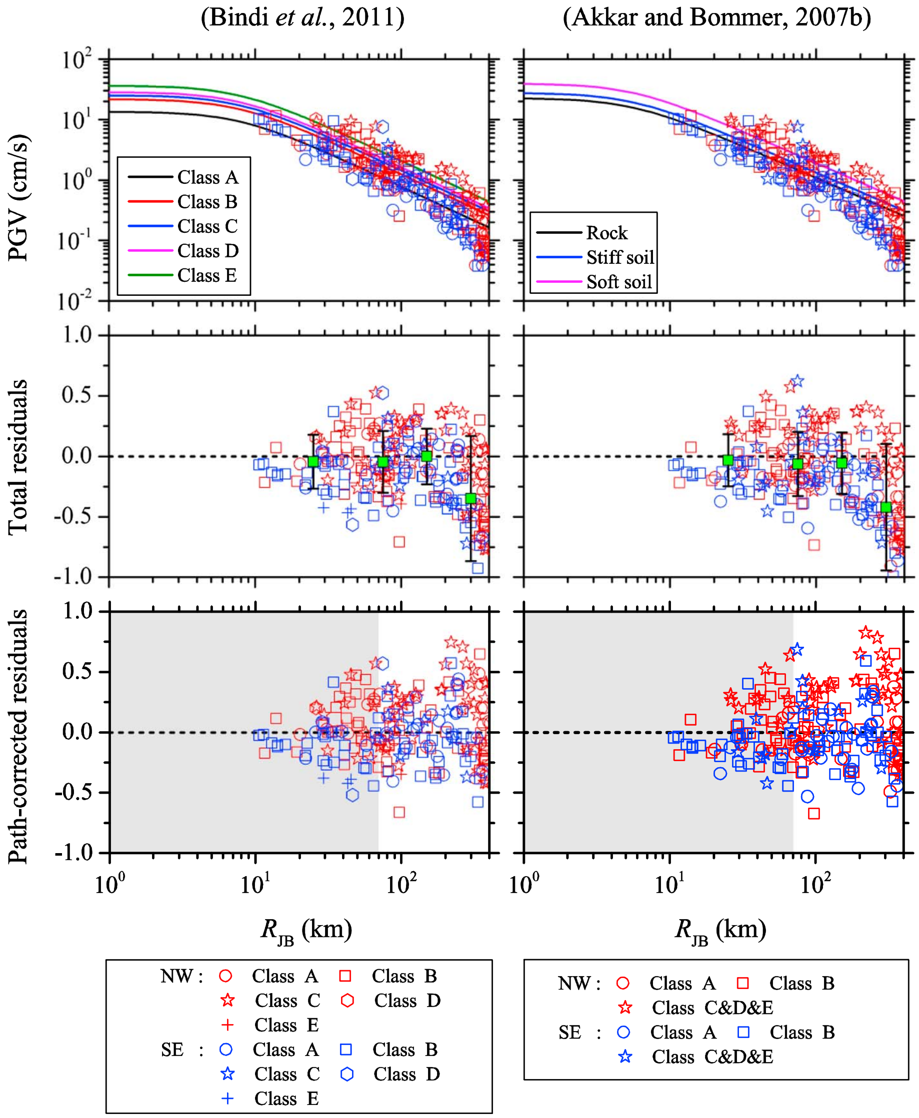

Figure 3. Same as Figure 2 but for PGV.

Figure 2 shows that the observed PGAs for $R_{JB} < 100$ km are consistent with the predicted medians, irrespective of whether calculated by Bin11 or AB07a. However, many of the observed values are below the predicted values for $R_{JB} > 100$ km, implying that the predicted PGAs given by both GPMEs are overestimated. It should be noted that the binned means of the total residuals calculated using Bin11 are smaller than those calculated using AB07a in the R_{JB} ranges of 100–200 and 200–400 km, indicating less overestimation by Bin11. As mentioned above, Bin11 was derived from the Italian strong motion database, which could guarantee more accurate estimations of ground motion within Italy. The PGV predictions of both Bin11 and AB07b do not show large systematic deviation in terms of distance dependence for $R_{JB} < 200$ km, unlike the PGA predictions in Figure 2. However, similar to PGA, both models overestimate the observed PGV when $R_{JB} > 200$ km.

Figures 2 and 3 illustrate that the path-corrected residuals are mostly positive in the NW sector and mostly negative in the SE sector for $R_{JB} < 70$ km, irrespective of the GMPE used. For $R_{JB} > 70$ km, the path-corrected residuals in the both NW and SE sectors are distributed uniformly around zero. This indicates that the observed PGAs and PGVs are generally larger in the NW sector than the SE sector for $R_{JB} < 70$ km. A tension spline interpolation method was used to obtain the spatial distributions of the path-corrected residuals of

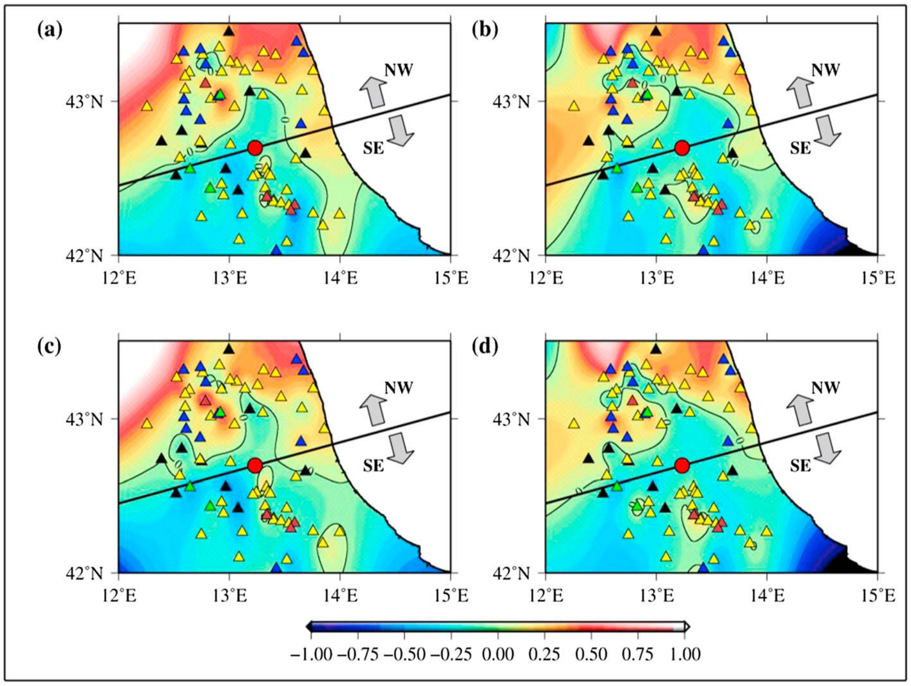

Figure 4. Spatial distributions of path-corrected residuals of PGAs using (a) Bin11 and (c) AB07a and PGVs using (b) Bin11 and (d) AB07b. The triangles in different colors indicating site classes, as in Figure 1, represent those stations with $R_{JB} < 70$ km considered in this study to investigate the directivity effects.

PGAs and PGVs for $R_{JB} < 70$ km, as shown in Figure 4. It is clear that the path-corrected residuals are mostly positive in the NW sector and mostly negative in the SE sector for $R_{JB} < 70$ km. The most likely reason for this is the rupture directivity effect; however, another potential reason could be local site effects. Although site effects were corrected for by the predicted IMs, they still could cause some differences between the IMs in the NW and SE sectors. In the GMPEs used in this study (i.e., Bin11, AB07a, and AB07b), the site class was considered when correcting for site effects. The correction factor was the same for all stations assigned as the same site class. However, the site class was assigned based on the V_{S30} range, e.g., stiff soil in the GMPEs of AB07a and AB07b corresponds to a wide range of V_{S30} (750 m/s $\leq V_{S30} \leq$ 360 m/s). This implies that even though stations might be assigned as the same site class, their site responses could have large variations.

To investigate the dependence of PGA and PGV on azimuth, Figure 5 shows the path-corrected residuals for PGAs and PGVs versus the event-to-site azimuth, as observed for $R_{JB} < 70$ km. It shows that for both PGA and PGV, most path-corrected residuals are larger than zero in the azimuth range of 255°–435° (NW sector) but less than zero in the azimuth range of 75°–255° (SE sector), implying strong dependence on the event-to-site azimuth. It should be noted that the path-corrected residuals are particularly large within the azimuth range of 300°–360°, corresponding to the NNW-SSE trend of the seismogenic fault. If rupture propagation were hypothetically predominant in this direction, it could explain the differences in the PGAs and PGVs in the NW and SE sectors as an effect of rupture directivity.

Figure 5 also presents the azimuthal variations of path-corrected residuals associated with different site classes. A mean of the path-corrected residuals with standard error was calculated for all sites classified as the same class. It shows that the path-corrected residuals for both PGA and PGV associated with different site classes have almost the same variation, and the mean of the path-corrected residuals for each site class is approximately close to zero, especially for Class B (most of the sites are classified as this class). This implies that the above mentioned differences of PGA and PGV in the two sectors are independent of local site effects. It should be noted that we calculated the mean of the path-corrected residuals with respect to Bin11 by combining Classes D and E together, because there are only three and four sites classified in these two classes, respectively (see Figure 1c).

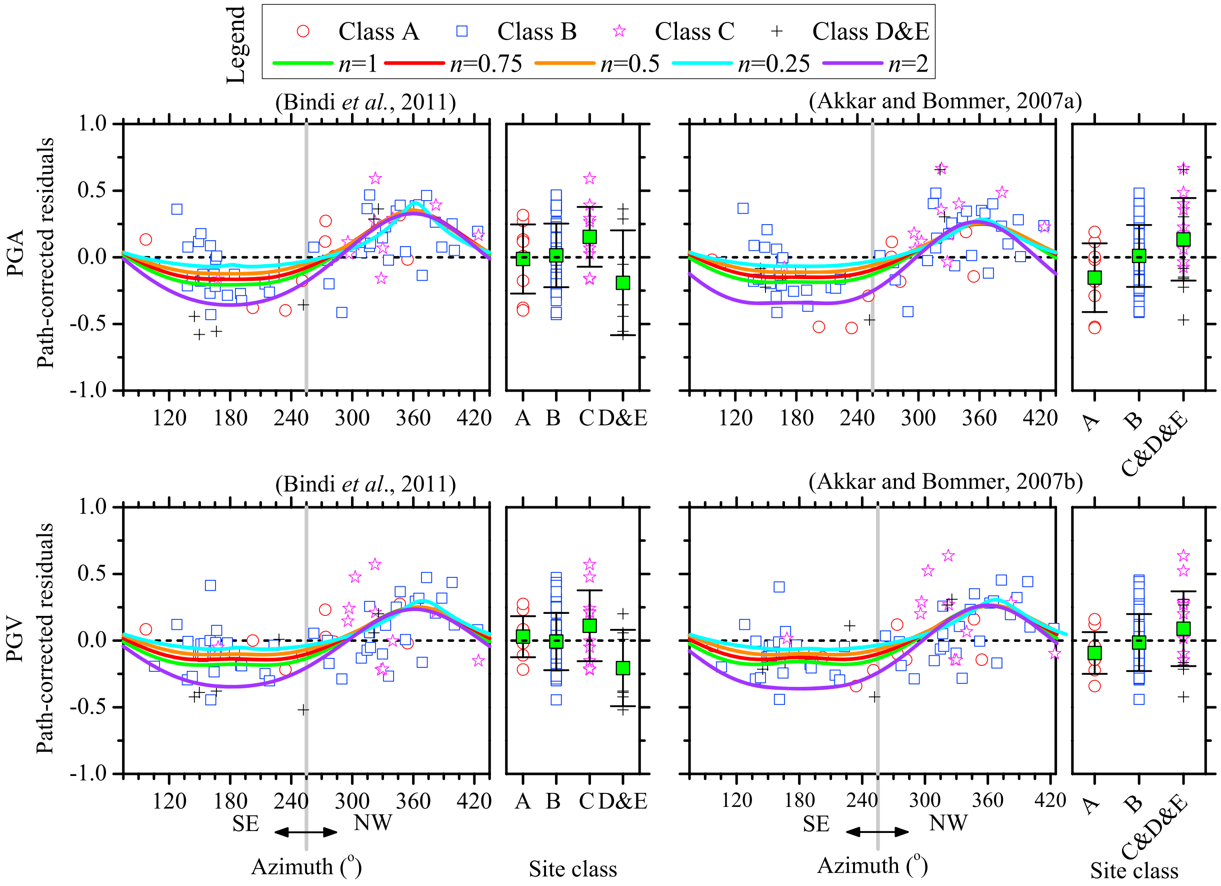

Figure 5. Path-corrected residuals for the observed PGAs and PGVs with $R_{JB} < 70$ km versus the event-to-site azimuth. A binned mean for each site class is represented using a green filled square with bars that indicate standard errors. The vertical gray line indicates a boundary separating the two station groups, i.e., NW and SE. To display a continuous distribution in the SE-NW direction, 360° is added to azimuths within the range 0°–75°. The colored lines representing base-10 logarithms of the directivity functions (i.e., $C_d^{\ n}$), based on the optimum source rupture parameters (Table 1), are compared with the path-corrected residuals of PGAs and PGVs.

3.2. Response Spectra

The total residuals of the 5% damped PSAs for both AB07a at periods of 0.05–4.00 s and Bin11 model at periods of 0.04–2.00 s were calculated for each site according to equation (1). The residuals for most stations in the NW sector are larger than in the SE sector, especially at periods of $T < 1.0$ s, as shown in Figure 6. Thus, the means of the residuals in the NW sector are all larger than in the SE sector, indicating that the observed PSAs in the NW sector are generally larger than in the SE sector, and at least twice as large for $T < 0.4$ s.

We selected two typical pairs of stations: FEMA and MSC, and CADA and MMP1, as shown in Figure 1b. For each pair, one station is located in the NW sector and the other in the SE sector. Both stations of each pair have the same site class (Class B), similar R_{JB}, and symmetrical distribution of azimuths (an approximate difference of 180°). The PSAs of each pair of stations are compared in Figure 7. It is evident that the PSAs observed at stations located in the NW sector are significantly larger than in the SE sector. The PSA observed at station FEMA is twice that observed at station MSC for periods of $T < 0.6$ s. The PSA observed at station CADA is about 3–5 times larger than station MMP1 for all periods ranging from 0.01 to 4.00 s. Excluding the influences of site and path attenuation, such considerable differences in PSA observed in the opposite sectors are most likely caused by source effects, e.g., rupture directivity.

To support the above explanation, we investigated the dependence of PSA at $T = 0.1$, 0.3, 0.5, 1.0, 1.5, and 2.0 s on the event-to-site azimuth, as shown in Figure 8. It should be noted that only sites located at $R_{JB} < 70$ km were considered, where the recorded PGAs and PGVs were strongly dependent on azimuth, as shown in Figure 5. The path-corrected residuals were calculated using the same approach adopted for the PGAs and PGVs. The predicted PSAs are given by Bin11 and AB07a, respectively. Figure 8 shows that

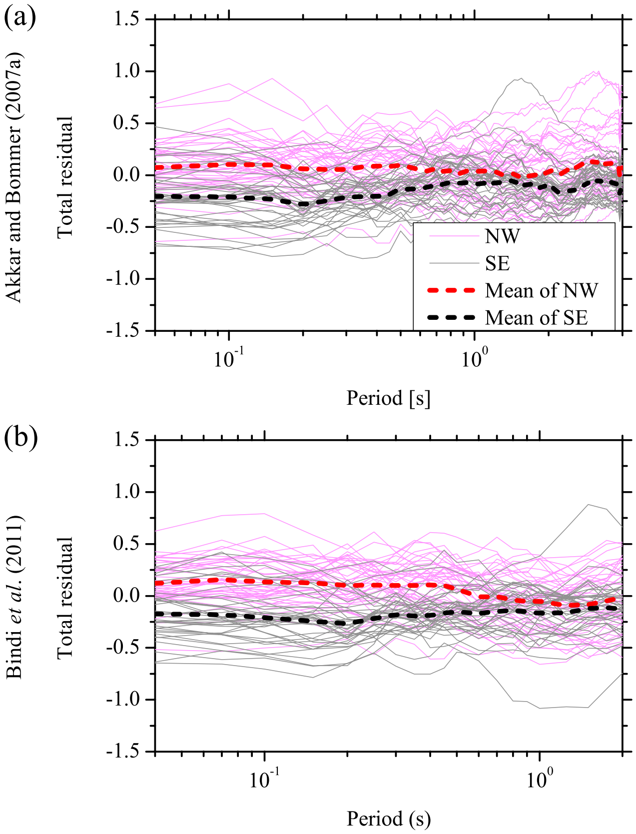

Figure 6. Comparison of the total residuals of pseudo spectral accelerations with 5% damping ratio in the NW and SE sectors (see legend). The residuals were calculated using GMPEs of (a) AB07a and (b) Bin11, respectively.

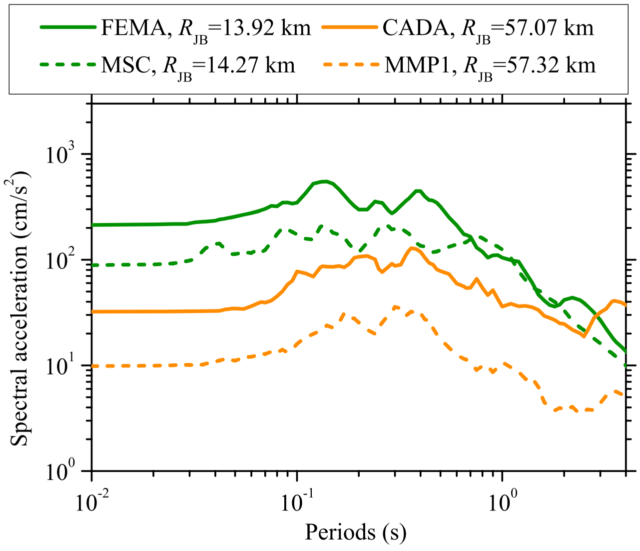

Figure 7. Comparison of the 5%-damped pseudo spectral accelerations for the two pairs of stations. Large differences in the spectral accelerations between the two stations of each pair are evident. The locations of both stations in each pair are symmetrical with respect to the boundary line between the NW and SE sectors, as shown in Figure 1b.

the path-corrected residuals derived from most sites in the NW sector are larger than zero for PSAs at $T = 0.1$, 0.3, and 0.5 s but less than zero for data derived in the SE sector. In particular, the path-corrected residuals are considerably positive in the azimuth range of 300°–360°, as found for PGA and PGV (see Figure 5). The same trend can be observed for the path-corrected residuals calculated using both Bin11 and AB07b. For PSA at T = 1.0, 1.5, and 2.0 s, such features cannot be observed clearly, implying that only the short-period ($T < 1.0$ s) PSAs observed in the NW sector are larger than observed in the SE sector, which could be attributable to rupture directivity.

4. Inverting Source Rupture Parameters

Using a technique proposed by Boatwright (2007) and Convertito et al. (2012), we inverted the azimuthally varying residuals for gross source rupture parameters, including rupture velocity, predominant rupture direction, and percent of unilateral rupture. This technique has been applied previously to investigate the rupture directions of three moderate earthquakes that occurred in northern Italy in 2012 (Convertito & Emolo, 2012) and four aftershocks of the M_S7.0 Lushan earthquake in China (Wen et al., 2015).

For a simple homogeneous kinematic line source model that ruptures bilaterally, the directivity amplification or deamplification of the spectral ordinate is proportional to $C_d{}^n$, where C_d is the directivity coefficient (Ben-Menahem, 1961; Boatwright, 2007; Hirasawa & Stauder, 1965):

$$C_d = \sqrt{\frac{k^2}{\left[1-\left(\frac{v_r}{c}\right)\cdot\cos\vartheta\right]^2}+\frac{(1-k)^2}{\left[1+\left(\frac{v_r}{c}\right)\cdot\cos\vartheta\right]^2}}, \tag{2}$$

where v_r/c is the Mach number (c is the shear-wave velocity and v_r is the rupture velocity) and ϑ is the angle between the ray that leaves the source and the direction of the rupture propagation (Joyner, 1991), which could be simply expressed as the rupture direction φ minus the event-to-site azimuth. Parameter k represents the relative portion of rupture length in the direction φ accounting for the entire rupture length. It constrains whether φ is the predominant rupture direction. Effectively, a value of $k > 0.5$ reveals that the rupture direction φ is predominant; otherwise, the opposite direction (i.e., φ + 180° or φ − 180°) is predominant.

The exponent n depends on the source model considered (Gallovič, 2017; Pacor et al., 2016; Ruiz et al., 2011), i.e., $n = 2$ for omega-squared kinematic models with single corner frequency and $n = 1$ for models with two corner frequencies (e.g., a linear model with constant slip and risetime). For models with heterogeneous distributions of slip and risetime or with incoherent rupture propagation, the value of n decreases from 2 or 1 to 0 in the case of purely stochastic and composite models. Generally, the exponent $n = 1$ is used to characterize the effect of rupture directivity on ground motions (Boatwright, 2007; Tan & Helmberger, 2010; Wen et al., 2015). Frequency-dependent n was also demonstrated by Pacor et al. (2016), who found it reproduced well the azimuthal distributions of apparent source spectra. It remains debatable which value of exponent n is optimum (Ruiz et al., 2011).

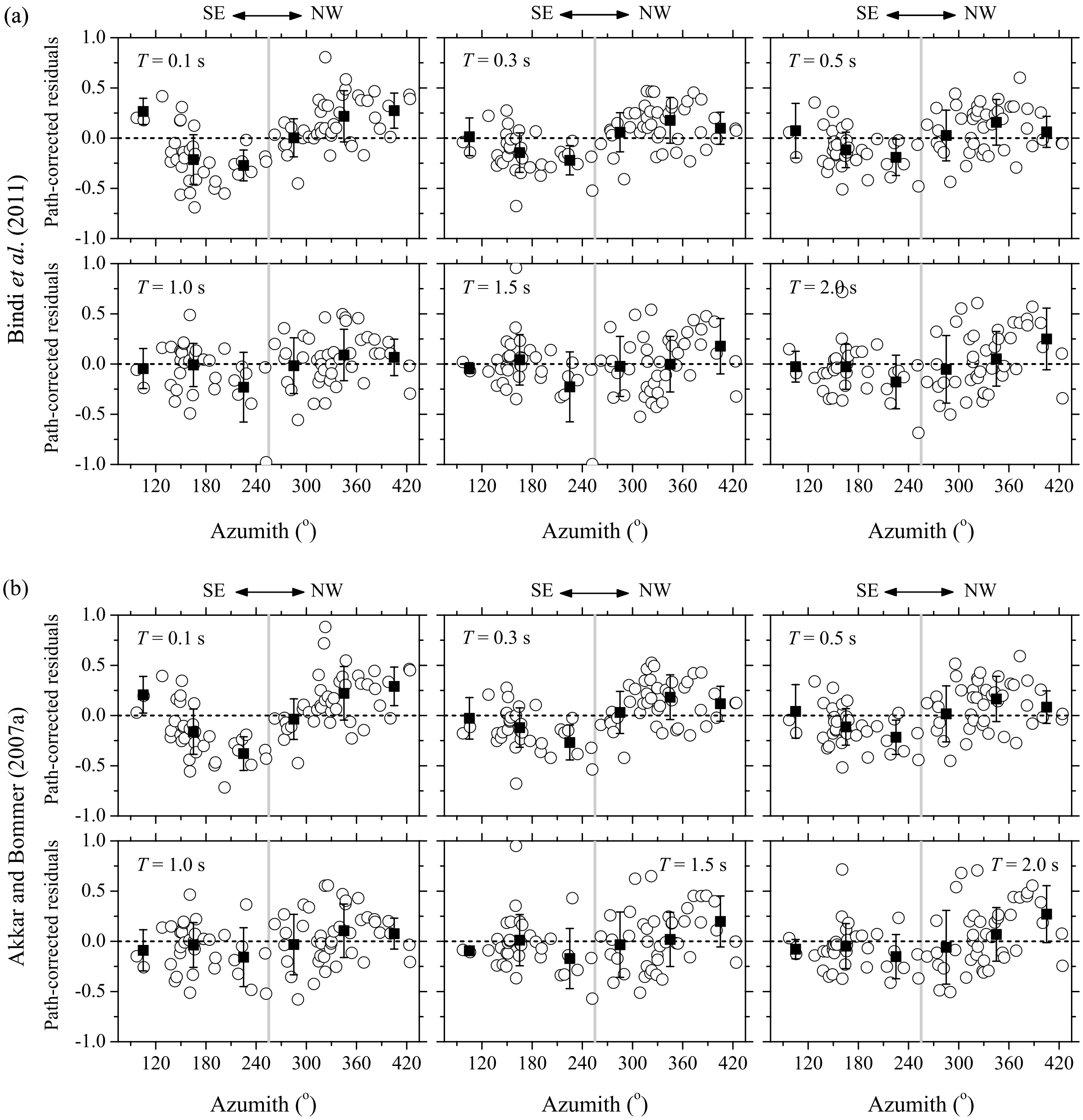

Figure 8. Path-corrected residuals versus event-to-site azimuths for spectral ordinates at periods T = 0.1, 0.3, 0.5, 1.0, 1.5, and 2.0 s for $R_{\mathrm{JB}} < 70$ km. The path-corrected residual is equal to the value of the total residual minus its distance-binned mean. The predicted PSAs are given by (a) Bindi et al. (2011) and (b) Akkar and Bommer (2007a). The azimuth-binned means are represented by the black squares with bars indicating standard errors.

The rupture directivity effect is not comprehensively considered in most GMPEs, including Bin11, AB07a, and AB07b. To eliminate the rupture directivity effect, the best fitted C_d parameters could be achieved theoretically to minimize the residuals between the theoretical predictions and the observed values corrected by $C_d{}^n$:

$$\sum_{i=1}^{N}\left[\log 10\left(Y_i^O/C_d^n\right)-\log 10\left(C_i^{\mathrm{un}}Y_i^P\right)\right]^2=\min, \tag{3}$$

where $Y_i{}^O$ and $Y_i{}^P$ represent the observed and predicted values, respectively, of PGA or PGV, and N means the number of strong motion recordings. The $C_i{}^{\mathrm{un}}$ term is a random variable that accounts for the uncertainties of the predicted values. The log10($C_i{}^{\mathrm{un}}$) term assumes a Gaussian distribution with zero mean and standard

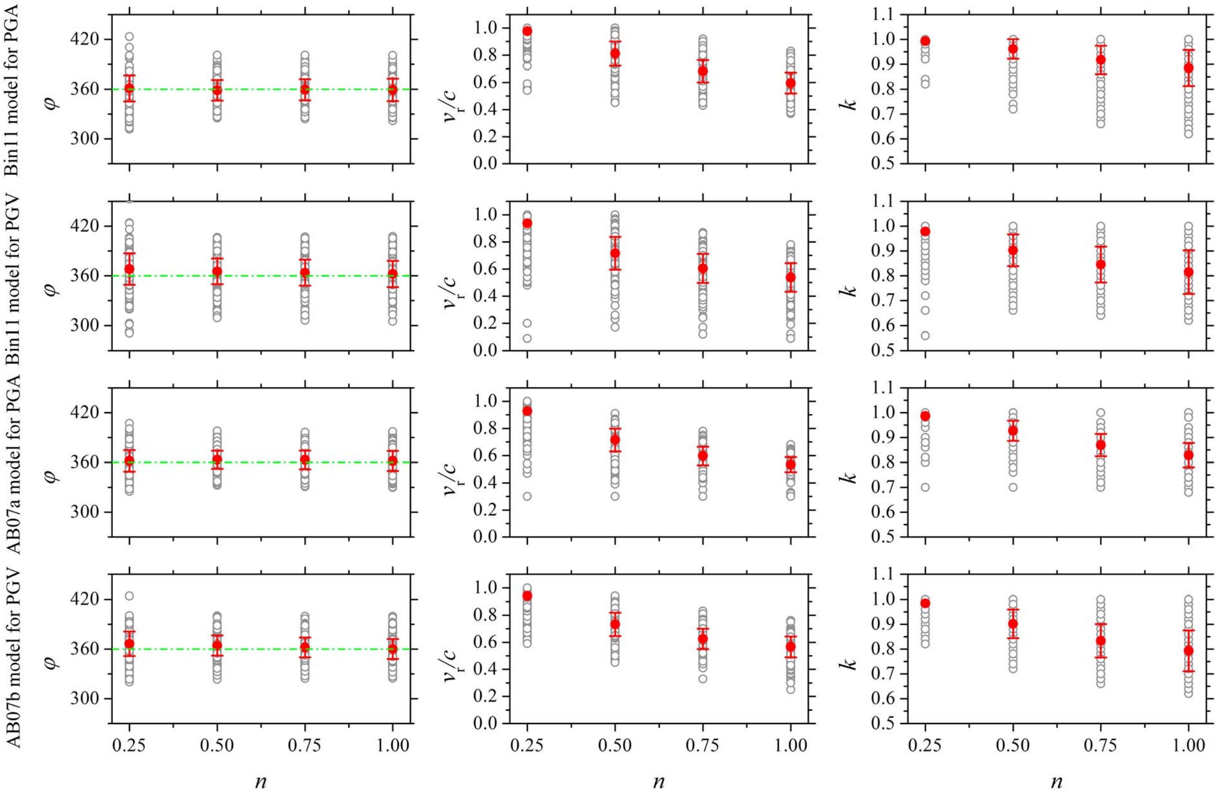

Figure 9. Optimal source rupture parameters for the cases of n = 0.25, 0.50, 0.75, and 1.00, including predominant rupture direction (φ), Mach number (v_r/c), and percent of unilateral rupture (k) derived from the 500 random realizations of the inversion. A mean for each parameter, averaged over all results from the 500 inversions, is represented using a red filled circle with bars that indicate the standard errors.

deviation equal to the total standard deviation of the GMPE. In equation (3), we tested n values fixed at 0.25, 0.50, 0.75, 1.00, and 2.00.

We used a grid-searching technique to obtain the optimum source parameters, including v_r/c, k, and φ. Bin11 was used in the inversion process for PGA and PGV, AB07a was used for PGA, and AB07b for PGV. Overall, 500 random realizations of inversion were made independently to derive 500 groups of optimal source rupture parameters, as shown in Figure 9. A Monte Carlo sampling technique was used to generate random variables of $\log10(C_i^{\mathrm{un}})$ (i = 1, N). The parameters that corresponded to the best fitting (i.e., mean) values, together with their uncertainties (standard deviations), are provided in Table 1.

The rupture directivity effects, described as C_d^n on the log10 scale, calculated using the mean values of φ, v_r/c, and k in Table 1, are plotted in Figure 5. Good agreements between C_d^n and the residuals of PGAs and PGVs are evident, except for the case of n = 2.00. The fitting thus supports the results of previous investigations suggesting that the rupture directivity effect could potentially have caused the large differences in the IMs observed in the NW and SE directions, i.e., the rupture forward and backward directions, respectively.

It is evident that the inverted parameters are similar whether using PGAs or PGVs in the case of the same value of n, irrespective of the GMPE. Furthermore, the standard deviation is small for each parameter, implying robust inversions. It should be noted that the standard deviations provided by the inversions using Bin11 are larger than those using AB07a and AB07b. This might be explained by the fact that the values of the standard deviations of PGA and PGV given by Bin11 are larger than given by AB07a and AB07b.

Figure 9 shows that the values of φ are independent of the exponent n, but both v_r/c and k are dependent. The rupture is predominantly unilateral, and the prevailing direction of rupture propagation has azimuth of ~360°, approximately close to the NNW-SSE trend of the seismogenic fault. The length of the major rupture was proportional to 70%–100% of the total ruptured fault. The smaller n value produced the larger percent of unilateral rupture. Figure 10 shows the epicenters of the aftershocks that occurred during the first 24 h after

Table 1
Seismic Source Rupture Parameters Inverted Using PGA and PGV

Exponent n	GMPE	Peak parameter	φ	v_r/c	k
1	Bin11	PGA	359.2 ± 13.4	0.59 ± 0.08	0.89 ± 0.07
	Bin11	PGV	362.3 ± 15.9	0.54 ± 0.11	0.81 ± 0.09
	AB07a	PGA	361.8 ± 11.8	0.53 ± 0.05	0.83 ± 0.05
	AB07b	PGV	360.0 ± 12.0	0.57 ± 0.08	0.79 ± 0.08
0.75	Bin11	PGA	359.4 ± 12.9	0.68 ± 0.08	0.92 ± 0.06
	Bin11	PGV	363.7 ± 15.7	0.60 ± 0.11	0.85 ± 0.07
	AB07a	PGA	363.1 ± 11.1	0.60 ± 0.07	0.87 ± 0.04
	AB07b	PGV	361.9 ± 11.9	0.63 ± 0.07	0.83 ± 0.07
0.5	Bin11	PGA	358.7 ± 12.4	0.81 ± 0.09	0.96 ± 0.04
	Bin11	PGV	365.3 ± 15.5	0.72 ± 0.12	0.90 ± 0.06
	AB07a	PGA	363.1 ± 10.7	0.72 ± 0.08	0.93 ± 0.04
	AB07b	PGV	364.2 ± 12.2	0.73 ± 0.09	0.90 ± 0.06
0.25	Bin11	PGA	361.1 ± 15.7	0.98[a]	0.99[a]
	Bin11	PGV	368.2 ± 19.0	0.93[a]	0.98[a]
	AB07a	PGA	361.9 ± 12.8	0.93[a]	0.98[a]
	AB07b	PGV	366.5 ± 15.0	0.94[a]	0.98[a]
2	Bin11	PGA	359.9 ± 15.1	0.39 ± 0.11	0.88 ± 0.13
	Bin11	PGV	361.2 ± 16.9	0.35 ± 0.15	0.85 ± 0.15
	AB07a	PGA	357.0 ± 15.7	0.43 ± 0.09	0.76 ± 0.11
	AB07b	PGV	360.1 ± 14.5	0.41 ± 0.15	0.80 ± 0.16

[a] The standard deviation is not included because of its small value.

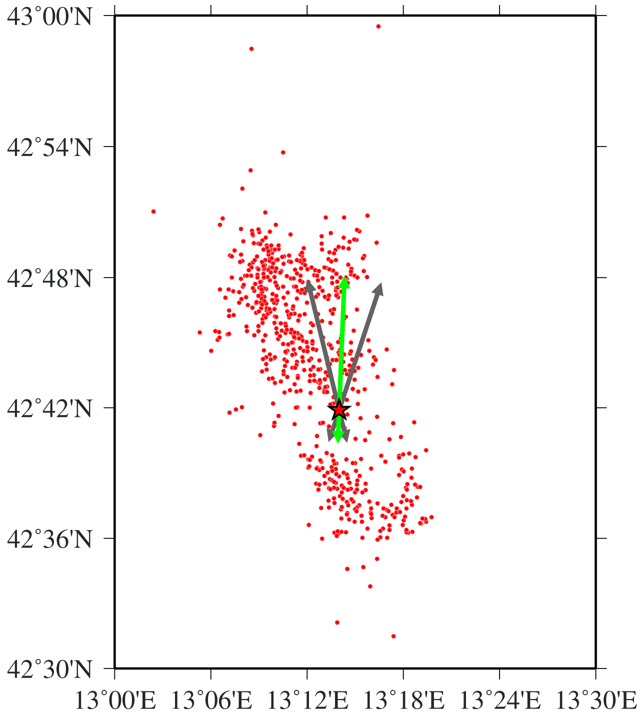

Figure 10. Aftershocks that occurred in the first 24 h after the main shock, and the predominant rupture direction inverted using the PGV equation of Bin11 for the case of $n = 1$. The green and gray arrows indicate the mean value and the range of one standard deviation, respectively, as presented in Table 1. The lengths of the arrows represent the rupture proportion, and they are not the actual rupture lengths in the respective directions. The red star and dots indicate the epicenters of the main shock and aftershocks, respectively. The catalog of aftershocks was downloaded from http://cnt.rm.ingv.it/.

the main shock and the rupture direction inverted using the PGV equation of Bin11 for the case of $n = 1$. It shows that the predominant rupture direction inverted in this study is almost consistent with the spatial distribution of aftershocks, implying that the inversion results are acceptable. It also agrees well with the rupture directivity toward the NNW derived from the kinematic rupture history provided by Tinti et al. (2016) and Pizzi et al. (2017). The optimum Mach number v_r/c varied in a wide range from ~0.5 to ~1.0, which depended strongly on the value of exponent n considered. A smaller value of exponent n resulted in a larger value of v_r/c. Values of v_r/c ranging from 0.7 to 0.9 are generally used by the seismology community; therefore, the values of 0.72–0.81 obtained for the case of $n = 0.5$ were considered. Results provided by Gallovič (2016) showed that the best fit with the observed near-fault strong motion data for frequencies greater than 1 Hz is provided by a model with n value of ~0.5. Given $c = 3.5$ km/s at the depth of 8 km (Herrmann, Malagnini, & Munafò, 2011), the rupture velocity determined was 2.52–2.84 km/s. This is close to the value of 2.8 km/s retrieved by Convertito, Matteis, and Pino (2017) and slightly lower than the values of 3.1 and 3.0 km/s given by Tinti et al. (2016) and Pizzi et al. (2017), respectively.

It should be noted that the uncertainty of earthquake magnitude might also affect the inversion results, because different values of Y_i^P in equation (3) could be derived using different earthquake magnitudes. For this Central Italy earthquake on 24 August 2016, different values of moment magnitude were measured, i.e., M_w6.2 by the U.S. Geological Survey and Pizzi et al. (2017), M_w6.1 by Tinti et al. (2016), and M_w6.0 by INGV. The value of M_w6.0 was adopted by Convertito et al. (2017) to investigate source directivity using a similar inversion method to this study, using a source model exponent of $n = 1.0$, and the Bin11 model for PGV prediction. They obtained similar values for φ and k but a larger value for v_r/c (~0.8) compared with the results of our study (v_r/c ~ 0.54). To investigate the influence of the uncertain value of M_w, values of 6.0, 6.1, and 6.2 were adopted separately to invert the rupture parameters for the case of $n = 1.0$, as shown in Figure 11. It shows that although the values of φ and k do have a little variability, significant variability is evident in the inverted v_r/c values. Given $M_w = 6.0$, v_r/c is equal to 0.72 ± 0.10, which is close to the value reported by Convertito et al. (2017).

5. Conclusions

Many strong motion recordings, obtained from RAN and RSN following the M_w6.2 earthquake that occurred in Italy on 24 August 2016, allowed us to investigate the imprint of rupture directivity based on ground motion IMs. The IMs used in this study included PGA, PGV, and 5% damped PSA. The recordings were separated into two groups (NW and SE) according to the source-to-site azimuth. The observed IMs were compared with predicted values estimated using different GMPEs, which were developed by Bindi et al. (2011) (called Bin11, for PGA, PGV, and PSA), Akkar and Bommer (2007a) (called AB07a, for PGA and PSA), and Akkar and Bommer (2007b) (called AB07b, for PGV). The path-corrected residual was calculated as the total residual between the observed and predicted values minus its distance-binned mean.

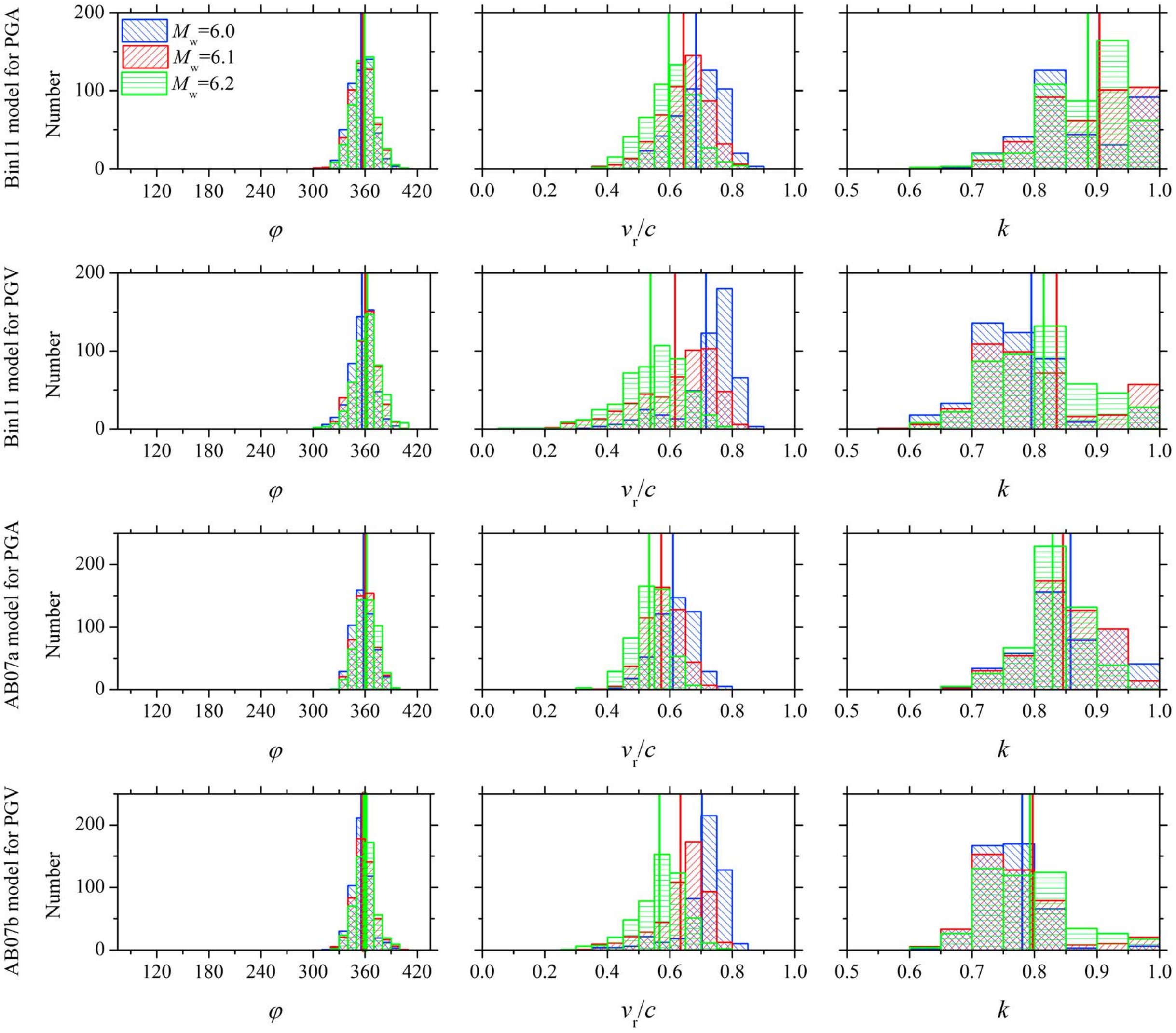

Figure 11. Histograms of the optimal source rupture parameters inverted by PGA and PGV for the case of exponent $n = 1$. The colors represent results inverted using different values of moment magnitude, i.e., 6.0, 6.1, and 6.2. The three vertical lines of different colors in each panel represent the mean of all results from 500 random realizations.

The dependence of the path-corrected residual on the event-to-site azimuth for $R_{JB} < 70$ km was investigated, and the following imprints of rupture directivity were determined.

1. The observed PGAs and PGVs in the NW sector were mostly larger than in the SE sector for $R_{JB} < 70$ km. For both PGA and PGV, most path-corrected residuals were larger than zero in the azimuth range of 255°–435° (NW sector) but less than zero in the azimuth range of 75°–255° (SE sector), indicating strong dependence of the path-corrected residuals on event-to-site azimuths. The path-corrected residuals were particularly large in the azimuth range of 300°–360°, which is approximately close to the NNW-SSE trend of the seismogenic fault. The mean of the path-corrected residuals, averaged over all sites of the same site class, was approximately close to zero, and the standard deviation was approximately constant, indicating that the rupture directivity effect rather than local site effects dominated the azimuthal variations of PGA and PGV.
2. The residuals of the PSAs in the NW sector were, in general, larger than in the SE sector, especially at periods of $T < 1.0$ s. The path-corrected residuals derived from sites located in the NW sector were mostly larger than zero for PSAs of $T = 0.1$, 0.3, and 0.5 s but less than zero for data derived in the SE sector. For PSAs of $T = 1.0$, 1.5, and 2.0 s, such a feature could not be observed clearly, implying that only short-period ($T < 1.0$ s) PSAs were affected by rupture directivity.

Finally, the observed PGAs and PGVs at stations with $R_{JB} < 70$ km were inverted for gross source rupture parameters, including rupture velocity, predominant rupture direction, and percent of unilateral rupture. The results showed that the rupture was predominantly unilateral, the major rupture was likely at an azimuth of ~360°, rupture velocity was 2.52–2.84 km/s, and the length of the major rupture was proportional to 70%–100% of the total ruptured fault, which is in agreement with slip inversion results (Pizzi et al., 2017; Tinti et al., 2016).

Acknowledgments

This work was supported by the Science Foundation of the Institute of Engineering Mechanics, CEA under grant 2016A04, National Natural Science Foundation of China U1534202 and 51308515 and National Science Foundation of Heilongjiang Province LC2015022. Strong-motion recordings used in this article were obtained from the Engineering Strong-Motion (ESM) database of ORFEUS at http://esm.mi.ingv.it/ (last accessed August 2017). Some of the plots were produced using Generic Mapping Tools (Wessel & Smith, 1991). We thank Laura Peruzza who is the Associate Editor, František Gallovič, and one anonymous reviewer for their valuable suggestions and constructive comments, which helped us to improve the manuscript.

References

Akinci, A., Malagnini, L., & Sabetta, F. (2010). Characteristics of the strong ground motions from the 6 April 2009 L'Aquila earthquake, Italy. *Soil Dynamics and Earthquake Engineering*, *30*, 320–335. https://doi.org/10.1016/j.soildyn.2009.12.006

Akkar, S., & Bommer, J. J. (2007a). Prediction of elastic displacement response spectra in Europe and the Middle East. *Earthquake Engineering and Structural Dynamics*, *36*, 1275–1301. https://doi.org/10.1002/eqe.679

Akkar, S., & Bommer, J. J. (2007b). Empirical prediction equations for peak ground velocity derived from strong-motion records from Europe and the Middle East. *Bulletin of the Seismological Society of America*, *97*, 511–530. https://doi.org/10.1785/0120060141

Al Atik, L., Abrahamson, N., Bommer, J. J., Scherbaum, F., Cotton, F., & Kuehn, N. (2010). The variability of ground- motion prediction models and its components. *Seismological Research Letters*, *81*, 794–801. https://doi.org/10.1785/gssrl.81.5.794

Benioff, H. (1955). Mechanism and strain characteristics of the White Wolf Fault as indicated by the aftershock sequence; Earthquakes in Kern County, California during 1952. *California Division of Mines Bulletin*, *171*, 199–202.

Ben-Menahem, A. (1961). Radiation of seismic surface-waves from finite moving sources. *Bulletin of the Seismological Society of America*, *51*(3), 401–435.

Bindi, D., Pacor, F., Luzi, L., Puglia, R., Massa, M., Ameri, G., & Paolucci, R. (2011). Ground motion prediction equations derived from the Italian strong motion database. *Bulletin of Earthquake Engineering*, *9*, 1899–1920. https://doi.org/10.1007/s10518-011-9313-z

Boatwright, J. (2007). The persistence of directivity in small earthquakes. *Bulletin of the Seismological Society of America*, *97*, 1850–1861. https://doi.org/10.1785/0120050228

Chiaraluce, L., Di Stefano, R., Tinti, E., Scognamiglio, L., Michele, M., Casarotti, E., … Marzorati, S. (2017). The 2016 Central Italy seismic sequence: A first look at the mainshocks, aftershocks, and source models. *Seismological Research Letters*, *88*(3), 757–771. https://doi.org/10.1785/0220160221

Cirella, A., Piatanesi, A., Tinti, E., Chini, M., & Cocco, M. (2012). Complexity of the rupture process during the 2009 L'Aquila, Italy, earthquake. *Geophysical Journal International*, *190*, 607–621. https://doi.org/10.1111/j.1365-246x.2012.05505.x

Convertito, V., Caccavale, M., De Matteis, R., Emolo, A., Wald, D., & Zollo, A. (2012). Fault extent estimation for near-real-time ground-shaking map computation purposes. *Bulletin of the Seismological Society of America*, *102*, 661–679. https://doi.org/10.1785/0120100306

Convertito, V., & Emolo, A. (2012). Investigating rupture direction for three 2012 moderate earthquakes in northern Italy from inversion of peak ground-motion parameters. *Bulletin of the Seismological Society of America*, *102*, 2764–2770. https://doi.org/10.1785/0120120067

Convertito, V., Matteis, R. D., & Pino, N. A. (2017). Evidence for static and dynamic triggering of seismicity following the 24 August 2016, $M_w = 6.0$, Amatrice (central Italy) earthquake. *Pure and Applied Geophysics*. *174*(10), 3663–3672. https://doi.org/10.1007/s00024-017-1559-1

Gallovič, F. (2016). Modeling velocity recordings of the M_w 6.0 South Napa, California, earthquake: Unilateral event with weak high-freqeuncy directivity. *Seismological Research Letters*, *87*(1), 2–14. https://doi.org/10.1785/0220150042

Gallovič, F. (2017). Azimuthal dependence of the ground motion variability from scenario modeling of the 2014 M_w6.0 South Napa, California, earthquake using as advanced kinematic source model. *Pure and Applied Geophysics*, *174*(9), 3467–3478. https://doi.org/10.1007/s00024-016-1424-7

Gallovič, F., Imperatori, W., & Martin Mai, P. (2015). Effect of three-dimensional crustal structure and smoothing constraint on earthquake slip inversions: Case study of the M_w6.3 2009 L'Aquila earthquake. *Journal of Geophysical Research: Solid Earth*, *120*, 428–449. https://doi.org/10.1002/2014/2014JB011650

Herrmann, R. B., Malagnini, L., & Munafò, I. (2011). Regional moment tensors of the 2009 L'Aquila earthquake sequence. *Bulletin of the Seismological Society of America*, *101*, 975–993. https://doi.org/10.1785/0120100184

Hirasawa, T., & Stauder, W. (1965). On the seismic body waves from a finite moving source. *Bulletin of the Seismological Society of America*, *55*(2), 237–262.

Hu, J. J., & Xie, L. L. (2011). Directivity in the basic parameters of the near-field acceleration ground-motions during the Wenchuan earthquake [in Chinese]. *Chinese Journal of Geophysics*, *54*, 2581–2589. https://doi.org/10.3969/j.issn.0001-5733.2011.10.015

Joyner, W. B. (1991). Directivity for non-uniform ruptures. *Bulletin of the Seismological Society of America*, *81*(4), 1391–1395.

López-Comino, J.-Á., de Lis Mancilla, F., Morales, J., & Stich, D. (2012). Rupture directivity of the 2011, M_w 5.2 Lorca earthquake (Spain). *Geophysical Research Letters*, *39*, L03301. https://doi.org/10.1029/2011GL050498

Pacor, F., Gallovič, F., Puglia, R., Luzi, L., & D'Amico, M. (2016). Diminishing high-frequency directivity due to a source effect: Empirical evidence from small earthquakes in the Abruzzo region, Italy. *Geophysical Research Letters*, *43*, 5000–5008. https://doi.org/10.1002/2016GL068546

Phung, V., Atkinson, G. M., and Lau, D. T. (2004), Characterization of directivity effects observed during 1999 Chi-Chi, Taiwan earthquake, 13th World Conference of Earthquake Engineering, Vancouver, B.C., Canada, 1–6 August 2004.

Pizzi, A., Domenica, A. D., Gallovič, F., Luzi, L., & Puglia, R. (2017). Fault segmentation as constraint to the occurrence of the main shocks of the 2016 Central Italy seismic sequence. *Tectonics*, *36*. https://doi.org/10.1002/2017TC004652

Ruiz, J. A., Baumont, D., Bernard, P., & Berge-Thierry, C. (2011). Modeling directivity of strong ground motion with a fractal, k^{-2}, kinematic source model. *Geophysical Journal International*, *186*, 226–244. https://doi.org/10.1111/j.1365-246x.2011.05000.x

Somerville, P. G., Graves, R. W., & Smith, N. F. (1996). Forward rupture directivity in the Kobe and Northridge earthquakes, and implications for structural engineering. *Seismological Research Letters*, *67*, 55.

Somerville, P. G., Smith, N. F., Graves, R. W., & Abrahamson, N. A. (1997). Modification of empirical strong ground motion attenuation relations to include the amplitude and duration effects of rupture directivity. *Seismological Research Letters*, *68*(1), 199–222. https://doi.org/10.1785/gssrl.68.1.199

Spudich, P., Rowshandel, B., Shahi, S. K., Baker, J. K., & Chiou, B. S. J. (2014). Overview and comparison of the NGA-West2 directivity models. *Earthquake Spectra*, *30*(3), 1199–1221. https://doi.org/10.1193/080313EQS222M

Tan, Y., & Helmberger, D. (2010). Rupture directivity characteristics of the 2003 Big Bear sequence. *Bulletin of the Seismological Society of America*, *100*, 1089–1106. https://doi.org/10.1785/0120090074

Tinti, E., Scognamiglio, L., Michelini, A., & Cocco, M. (2016). Slip heterogeneity and directivity of the ML 6.0, 2016, Amatrice earthquake estimated with rapid finite-fault inversion. *Geophysical Research Letters*, *43*, 10,745–10,752. https://doi.org/10.1002/2016GL071263

Velasco, A. A., Ammon, C. J., & Lay, T. (1994). Empirical Green function deconvolution of broadband surface waves: Rupture directivity of the 1992 Landers, California (M_w = 7.3), earthquake. *Bulletin of the Seismological Society of America*, *84*(3), 735–750.

Wen, R. Z., Wang, H. W., & Ren, Y. F. (2015). Rupture directivity from strong-motion recordings of the 2013 Lushan aftershocks. *Bulletin of the Seismological Society of America*, *105*(6), 3068–3082. https://doi.org/10.1785/0120150100

Wessel, P., & Smith, W. H. F. (1991). Free software helps map and display data. *Eos, Transactions American Geophysical Union*, *72*(41), 441. https://doi.org/10.1029/90EO00319